JGR Oceans

RESEARCH ARTICLE
10.1029/2024JC021929

The 20-Year Highest Tropical Cyclone-Generated Waves Associated With the Maximum Energy of Seismic Noises

Tomoya Shimura[1], **Masumi Yamada**[1], **Nobuhito Mori**[1], and **Takuya Miyashita**[1]

[1]Disaster Prevention Research Institute, Kyoto University, Kyoto, Japan

Key Points:

- 20-year long microseisms observations around Japan and high-resolution ocean wave hindcast were statistically analyzed
- The three events with the highest microseism energy in the period of 8–10 s were Typhoon Wipha in 2013, Lan in 2017, and Hagibis in 2019
- The microseisms events were associated with the highest wave heights and the largest wave-induced pressures generated by tropical cyclones

Correspondence to:

T. Shimura,
shimura.tomoya.2v@kyoto-u.ac.jp

Citation:

Shimura, T., Yamada, M., Mori, N., & Miyashita, T. (2025). The 20-year highest tropical cyclone-generated waves associated with the maximum energy of seismic noises. *Journal of Geophysical Research: Oceans*, *130*, e2024JC021929. https://doi.org/10.1029/2024JC021929

Received 1 OCT 2024
Accepted 2 JAN 2025

Author Contributions:

Conceptualization: Tomoya Shimura
Data curation: Tomoya Shimura, Masumi Yamada
Formal analysis: Tomoya Shimura, Masumi Yamada, Nobuhito Mori, Takuya Miyashita
Funding acquisition: Tomoya Shimura
Investigation: Tomoya Shimura
Methodology: Tomoya Shimura
Resources: Tomoya Shimura
Software: Tomoya Shimura
Visualization: Tomoya Shimura
Writing – original draft: Tomoya Shimura, Masumi Yamada, Nobuhito Mori, Takuya Miyashita
Writing – review & editing: Tomoya Shimura, Masumi Yamada, Nobuhito Mori, Takuya Miyashita

Abstract The extreme winds of tropical cyclones generate high waves over the ocean, causing severe damage to offshore facilities and coastal communities. Disaster mitigation requires accurate prediction and forecasting of the highest potential waves. However, the physics of wave development is not fully understood, and the number of mid-ocean observations during extreme tropical cyclones is extremely insufficient. Therefore, physically and statistically evaluating the highest potential waves is difficult. However, ocean waves excite seismic noise (microseisms). Although source sites of microseisms under specific tropical cyclones have been identified by case studies, the extreme ocean wave magnitude under tropical cyclones have not been systematically analyzed using long-term historical records. Here, we, for the first time, utilize long-term microseisms observed by seismic observation networks to associate the historical maximum microseisms events with the highest tropical cyclone-generated wave events around Japan. We show that Typhoon Wipha in 2013, Typhoon Lan in 2017, and Typhoon Hagibis in 2019 were the maximum microseisms events in the past 20 years based on microseism energy within an 8–10 s period. We associate the events with the highest wave heights and the largest wave-induced sea surface pressures generated by tropical cyclones. Although ocean wave models have a large uncertainty of tropical cyclone-generated extreme waves, microseisms observations can endorse the results of an ocean wave model even if lack of direct ocean wave observation under tropical cyclones. Furthermore, rich information of microseisms on wave development and propagation has a potential to proceed understanding of the extreme wave physics.

Plain Language Summary The extreme winds of tropical cyclones generate high ocean waves, causing severe damage to offshore facilities and coastal communities. Accurate prediction and forecasting of worst-class high waves are essential for disaster mitigation. However, the mechanism behind extreme ocean wave development is not fully understood, and mid-ocean observations during extreme tropical cyclones are extremely limited due to the challenges of conducting such observations. This lack of data hinders the physical and statistical evaluation of worst-class high waves. On the other hand, ocean waves can induce ground vibrations, known as microseisms, which can propagate over long distances. In this study, we utilize long-term microseisms observed by seismic networks to identify the historical highest wave events generated by tropical cyclones around Japan. Our findings indicate that Typhoon Wipha in 2013, Typhoon Lan in 2017, and Typhoon Hagibis in 2019 were among the most extreme events of the past 20 years. Microseisms provide a valuable method for validating ocean wave models, even without direct wave observations, and offer rich insights into the development and propagation of waves, which can improve our understanding of the mechanisms behind the highest-class waves.

1. Introduction

Extreme ocean surface waves from tropical cyclones and storm surges cause tremendous coastal disasters in low to middle latitudes (Rappaport, 2014). An accurate estimation of extreme ocean waves that develop under tropical cyclones is required to assess and plan disaster mitigation. However, the highest-class waves under tropical cyclones are rarely observed, owing to the sparse observation of ocean waves (Shimura et al., 2024). Furthermore, the wave observation locations are limited to coastal areas, although severe waves develop offshore. Wave development, an entity of momentum loss from a tropical cyclone, determines the intensity of the tropical cyclone (Emanuel, 1988). Therefore, understanding of wave development is important for meteorological point of view as well.

Ocean surface waves excite small seismic waves known as seismic noise (microseisms). The generation theory is explained by the wave-topography interaction and second-order pressure variation in two ocean waves traveling

in opposite directions (Ardhuin & Herbers, 2013; Ardhuin et al., 2012; Hasselmann, 1963; Longuet-Higgins, 1950). An interaction between waves and topography generates primary microseisms at the same frequency as waves with peaks at approximately 10–30 s. Secondary microseisms that appear twice frequency as waves with peaks at approximately 5–7 s are generated by interactions between waves traveling in opposite directions (Nakata et al., 2019). The relationship between microseisms and ocean waves was analyzed based on seismic observations and ocean wave observations/computational hindcasts (Ardhuin et al., 2011; Bromirski et al., 2005; Gualtieri et al., 2019; Poppeliers & Mallinson, 2015; Takagi et al., 2018; Traer et al., 2012). Currently, seismic observations are spatially 100 times denser on land in earthquake-prone areas and have a longer history (>100 years) than ocean-wave monitoring. Therefore, seismic observations can provide ocean wave information for regions and periods without ocean wave observations (Aster et al., 2023; Bromirski, 2023; Grevemeyer et al., 2000).

It has been known that the microseism observation can detect tropical cyclone existence (Algué, 1900; Gilmore & Hubert, 1948). The source sites of microseisms generated at the mid-ocean under a specific tropical cyclone (e.g., Typhoon Loke in 2006) have been located using seismic data (Fan et al., 2019; Nishida & Takagi, 2022; Retailleau and Gualtieri, 2019, 2021; Traer et al., 2012; Zhang et al., 2010). Gualtieri et al. (2018) identified the source locations and constructed the statistical prediction model of tropical cyclone (wind speed) intensity from microseisms. Microseisms are excited by ocean waves generated by tropical cyclones and not the tropical cyclones itself (Lin et al., 2017; Park & Hong, 2020; Sufri et al., 2014). Previous studies on microseisms excited by tropical cyclones (and generated ocean waves) have focused on detecting seismic source locations of specific tropical cyclones, but information on the magnitude/intensity of ocean waves under tropical cyclones which is greater interest of disaster mitigation and research on extreme wave physics, is lacking. Such studies refer to the global ocean wave hindcast/reanalysis forced by global atmospheric reanalysis with a spatial resolution of approximately 0.5° spatial resolution (Lin et al., 2017; Nishida & Takagi, 2022; Park & Hong, 2020; Sufri et al., 2014; Traer et al., 2012), and the global data are too coarse to reproduce extreme tropical cyclone winds and the resultant waves. Furthermore, systematic long-term studies on microseisms, including the historical highest wave events, are lacking, although several case studies of specific tropical cyclones are available.

Direct ocean wave observations cannot identify the highest-class historical ocean wave events generated by tropical cyclones because of the limited number of observations in coastal areas (although the swell radiated from tropical cyclones provide useful indirect observation). This study associates the historical highest-class ocean wave events generated by tropical cyclones with microseisms based on statistical analysis on the long-term seismic observations and high-resolution (and therefore tropical cyclone-captured) ocean wave simulations. This study targeted secondary microseisms (2–10 s) observed by the Japanese on-land and ocean-bottom seismic observation networks during the summer (July–October) of the past 20 years.

2. Methodology

2.1. Seismic Observation Data

Data from well-organized nationwide Japanese seismic observation networks have been consistently available over the past 20 years. The Japanese nationwide broadband seismograph network maintained by the National Research Institute for Earth Science and Disaster Resilience (NIED), the so-called Full Range Seismograph Network of Japan (F-net; Okada et al., 2004; NIED F-net, 2019), was used for seismic observation data. F-net consists of broadband and strong-motion seismographs. Data from broadband seismographs were analyzed in this study. The F-net is an on-land observation network. In addition to F-net, the ocean-bottom observation network of broadband seismographs from DONET (Dense Ocean floor network system for Earthquakes and Tsunamis; NIED DONET, 2019) maintained by NIED was added to the analysis. The broadband seismic data sampling rate from F-net and DONET was 100 Hz. The maximum data periods in this study were 2004–2023 for F-net and 2015–2023 for DONET, depending on the location. The maximum data length was 20 years for the F-net and 7–8 years for the DONET. Only data from summer (July to October), the active typhoon season, were used. Figure 1a shows the locations of the seismic stations and the data length.

2.2. Definition of Microseism Magnitude

The magnitude of the microseisms was defined by integrating the power spectral density (PSD) of the vertical displacement within a specific frequency band of secondary microseisms. First, the PSD was calculated using

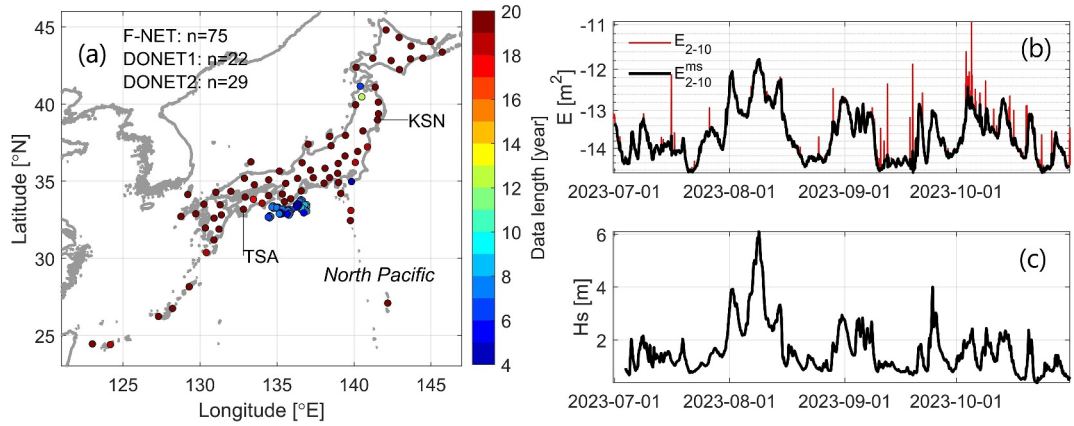

Figure 1. Explanation of the data. (a) Locations of seismic stations. The color scale represents the data length (years). The data at stations TSA and KSN are used as the representative locations for western and eastern locations, respectively. (b) Example of earthquake signal elimination at the seismic station TSA during summer 2023 (Red line is raw signal and black line is signal after elimination). (c) The time series of simulated wave height H_s at a location 75 km south of the location of seismic station TSA.

Welch's method to a 1-hr long 100 Hz-sampled vertical velocity data with a 5-min segment and 50% overlap. The PSD of the velocity was converted to the displacement by dividing it by the square angular frequency. The energy integrated within a specific band (t_1 to t_2) was denoted as $E_{t_1-t_2}(t,x) = \log_{10} \int_{1/t_2}^{1/t_1} PSD(t,x,f)\, df$, where t is the time, x is the observed location, and f is the frequency. $E_{t_1-t_2}(t,x)$ represents hourly data. A third-order median filter was applied to the time series of $E_{t_1-t_2}$ for noise elimination at first.

In this study, the earthquake signal in $E_{t_1-t_2}$ was treated as noise. The earthquake signal was eliminated from $E_{t_1-t_2}$ systematically as follows: First, the earthquake signals were defined. Focusing on data at a certain time (t) and location (x), the mean value between $t \pm r$ h is as follows:

$$E_{t_1-t_2}(t,x)_i = E_{t_1-t_2}(t-r+i,x) \tag{1}$$

$$E^{\text{mean}}_{t_1-t_2}(t,x) = \frac{1}{2r+1} \sum_{i=1}^{2r+1} E_{t_1-t_2}(t,x)_i. \tag{2}$$

Subtracting the mean value from each data can be written as follows:

$$E'_{t_1-t_2}(t,x)_i = E_{t_1-t_2}(t,x)_i - E^{\text{mean}}_{t_1-t_2}(t,x). \tag{3}$$

The earthquake signal is defined as follows:

$$E^{eq}_{t_{eq1}-t_{eq2}}(t)_i = \underset{x}{\text{median}}\left(E'_{t_{eq1}-t_{eq2}}(t,x)_i\right) \tag{4}$$

where $t_{eq1} - t_{eq2}$ is the period range for defining the earthquake signal and $\underset{x}{\text{median}}()$ is the median value over all observation locations of F-net. This assumes that the shape of the time series of earthquakes is similar over Japan, north to south and west to east, compared to microseisms. The vector form of $E^{eq}_{t_1-t_2}(t)_i$ can be represented as follows:

$$\boldsymbol{E}^{eq}_{t_{eq1}-t_{eq2}}(t) = \left(E^{eq}_{t_{eq1}-t_{eq2}}(t)_1, \cdots, E^{eq}_{t_{eq1}-t_{eq2}}(t)_{2r+1}\right) \tag{5}$$

where $\boldsymbol{E}^{eq}_{t_1-t_2}(t)$ has $2r+1$ components. The earthquake signal was then eliminated, and the microseism signal was constructed as follows:

$$E^{ms}_{t_1-t_2}(t,x)_i = E'_{t_1-t_2}(t,x)_i - \left\{aE^{eq}_{t_{eq1}-t_{eq2}}(t)_i + b\right\} + E^{\text{mean}}_{t_1-t_2}(t,x) \quad (6)$$

where a and b are determined by the least square method for the regression of $\boldsymbol{E}'_{t_1-t_2}(t,x)$ on $\boldsymbol{E}^{eq}_{t_{eq1}-t_{eq2}}(t)$. After elimination, only the $(r+1)$ th value, $E^{ms}_{t_1-t_2}(t,x)_{r+1}$, was used as microseismic data. The period band of 20–30 s was used for $t_{eq1}-t_{eq2}$ because the ocean wave periods were mainly less than 20 s. r was set to 12 hr. After the elimination of the earthquake signal, the data cap was corrected by eliminating the data with less than −1.5, the standard deviation, and the mean of the 1-month segment was greater than twice the standard deviation. Figure 1b shows an example of the results of earthquake signal elimination, plotting the time series of raw data $E_{2-10}(t,x)$ and $E^{ms}_{2-10}(t,x)_{r+1}$ for 2023 at a certain location (location number TSA shown in Figure 1a). Evidently, the spike was successfully eliminated. $E_{t_1-t_2}(t,x)$ denotes $E^{ms}_{t_1-t_2}(t,x)_{r+1}$ hereafter. Regarding DONET, $\boldsymbol{E}^{eq}_{t_{eq1}-t_{eq2}}(t)$ is the same as that of F-net.

2.3. Ocean Surface Wave Hindcast

Ocean surface wave hindcasting was conducted using the spectral wave model WAVEWATCH III version 7 (The WAVEWATCH III Development Group, 2019). The computational domains were the Western North Pacific domain (120.25° E to 154.69° E and 22.50° N to 47.50° N), nested in the North Pacific domain (110° E to 90.25° W and 25° S to 65° N). The spatial resolution of the inner domain was approximately 5 km, whereas that of the outer domain was 0.25 °. WAVEWATCH III was forced by ocean surface winds from the hourly operational analysis data of the Japanese Meteorological Agency's Meso Scale Model (JMA-MSM; JMA, 2024) for the inner domain and JRA-55 reanalysis (Kobayashi et al., 2015) for the outer domain. The ocean current data was not used in this study although the Kuroshio current has some impacts on waves (Alday et al., 2021). The spatial resolutions of the JMA-MSM and JRA-55 were 5 and 60 km, respectively. The widely used parametrization of the wind input/dissipation source term (ST4; Ardhuin et al., 2010) was selected from WAVEWATCH III. The directional resolution was 10°, and the frequency domain was discretized by 36 within 0.035–0.98 Hz. The shoreline energy reflection coefficient was set to $R^2 = 0.1$ (Ardhuin & Roland, 2012). Unlike previous studies using global models with a spatial resolution of approximately 0.5° (Lin et al., 2017; Nishida & Takagi, 2022; Park & Hong, 2020; Sufri et al., 2014), both atmospheric and wave models had a higher resolution (5 km); therefore, it was considered that the magnitudes of tropical cyclone-generated waves were captured better.

One of the wave parameters used in this study is the significant wave height (H_s). H_s is defined as follows:

$$H_s = 4\sqrt{\int\int F(f,\theta)\,df\,d\theta} \quad (7)$$

where $F(f,\theta)$ is wave spectrum, f is a wave frequency, and θ is a wave direction. Equation 7 indicates that H_s is derived from the total wave energy as follows: Figure 1c shows the time series of the simulated H_s at a location 75 km away from the TSA seismic station (Figure 1a), indicating a correspondence between waves (Figure 1c) and microseisms (Figure 1b). In addition to H_s, we introduced the H_s derived from the limited energy within a specific frequency as follows:

$$H_{t_1-t_2} = 4\sqrt{\int\int_{\frac{1}{2t_2}}^{\frac{1}{2t_1}} F(f,\theta)\,df\,d\theta.} \quad (8)$$

Here, because we considered secondary microseisms, twice periods ($2t$) were used in Equation 8. For example, H_{2-10} was derived from the energy within the wave frequency domain of 1/4–1/20 Hz. Furthermore, the second-order pressure variance that contributes to secondary microseisms (Nakata et al., 2019) is represented by

$$P_s(2f) = \int (2f)\left\{\int F(f,\theta)d\theta\right\}^2 I(f)\,df \quad (9)$$

$$I(f) = \int_0^{\pi} \frac{F(f,\theta)\,F(f,\theta+\pi)}{\left\{\int F(f,\theta)d\theta\right\}^2} d\theta \tag{10}$$

Equations 9 and 10 represent the magnitude of the wave energy of the wave components traveling in opposite directions. Similar to the wave heights, the integrated pressure within a specific band is defined as follows:

$$P_{t_1-t_2} = \int_{\frac{1}{t_2}}^{\frac{1}{t_1}} P(2f)\,df \tag{11}$$

The data size $F(f,\theta)$ is large. Therefore, the data $F(f,\theta)$ was output every 20 km and the output of $H_{t_1-t_2}$ had a 20 km spacing. The remaining were placed on a native computational grid (5 km). Every output was hourly.

3. Results

3.1. The Correlation Between Ocean Wave Heights and Microseisms

First, we show how microseisms correlate with ocean waves at the Japanese scale. The correlation coefficients between hourly $E_{t_1-t_2}$ and H_s or $H_{t_1-t_2}$ were calculated. For example, Figure 2a shows the spatial distribution of correlation coefficients between hourly E_{2-10} at location (TSA) and hourly H_s of each grid point of the wave simulations during the summer from 2004 to 2023. E_{2-10} and H_s were highly correlated, with a maximum correlation coefficient of 0.82. The location of the maximum correlation was 75 km south of the seismic station. The correlation coefficient shown in Figure 2a decays as a function of distance from the station. Therefore, microseisms with a wider range E_{2-10} is mainly excited by waves in the region closer to the seismic station.

Waves grow due to wind, resulting in higher wave heights and longer wave periods (Hasselmann et al., 1973). The long-period component of microseisms (8–10 s), the correlation coefficients of E_{8-10} with H_{8-10} were lower than those of E_{2-10}, as shown in Figure 2b. The maximum value was 0.68. The reason for the lower correlation is that waves with high H_{8-10} (16–20 s period wave components) do not occur frequently in summer in the western North Pacific. Basically, high H_{8-10} are generated by tropical cyclones in this region (Shimura & Mori, 2019). Therefore, during the period of no tropical cyclones, E_{8-10} and H_{8-10} are small and lower than the noise level, and the correlation decreases.

The tropical cyclone events are focused here. A total of 207 tropical cyclones passed through the domain over 20 years. The maximum value of hourly $E_{t_1-t_2}$ for each tropical cyclone event and each seismic station was obtained. For H_s and $H_{t_1-t_2}$, the maximum values for each computational grid point were obtained. Considering the spatial extent of wave events, the averaged values of the maximum wave heights within the region of correlation coefficients greater than 0.5 (Figures 2a and 2b) were calculated. Figure 2c shows the relationship between the maximum E_{2-10} at the TSA location and the spatially averaged maximum H_s during tropical cyclone events. Figure 2d is the same as Figure 2c, but for the long-period components (E_{8-10} and H_{8-10}). Figures 2c and 2d indicates high correlations between the microseisms and wave heights for wider- and long-period components. The correlation coefficients between E_{2-10} and H_s and between E_{8-10} and H_{8-10} were 0.86 and 0.84, respectively (Figures 2c and 2d). By focusing on severe wave conditions under tropical cyclones and considering the spatial extent, the correlation of the long-period components was higher (Figure 2d) compared to that without limitation and spatial extension (Figure 2b). The above results are only for a single seismic station in the TSA. The correlation coefficients for all seismic stations were calculated similarly. Figures 2e and 2f shows the correlation coefficients for secondary microseisms with wider-range and long-period components at all seismic stations. The correlation coefficients at almost all stations were more than 0.8 between E_{2-10} and H_s (Figure 2e). For the long-period components, high correlation was observed between E_{8-10} and H_{8-10} (Figure 2f). The correlation coefficients in the southern part were more than 0.8 for almost all stations. This can be because the southern part is closer to the region of frequent tropical cyclone area and the microseisms at the southern part are dominated by tropical cyclone events. The reason why the correlation coefficient at the northern part is smaller than southern part can be because the distance to frequent tropical cyclone region is greater and the wave affecting microseisms is constrained by eastern boundary of computational domain.

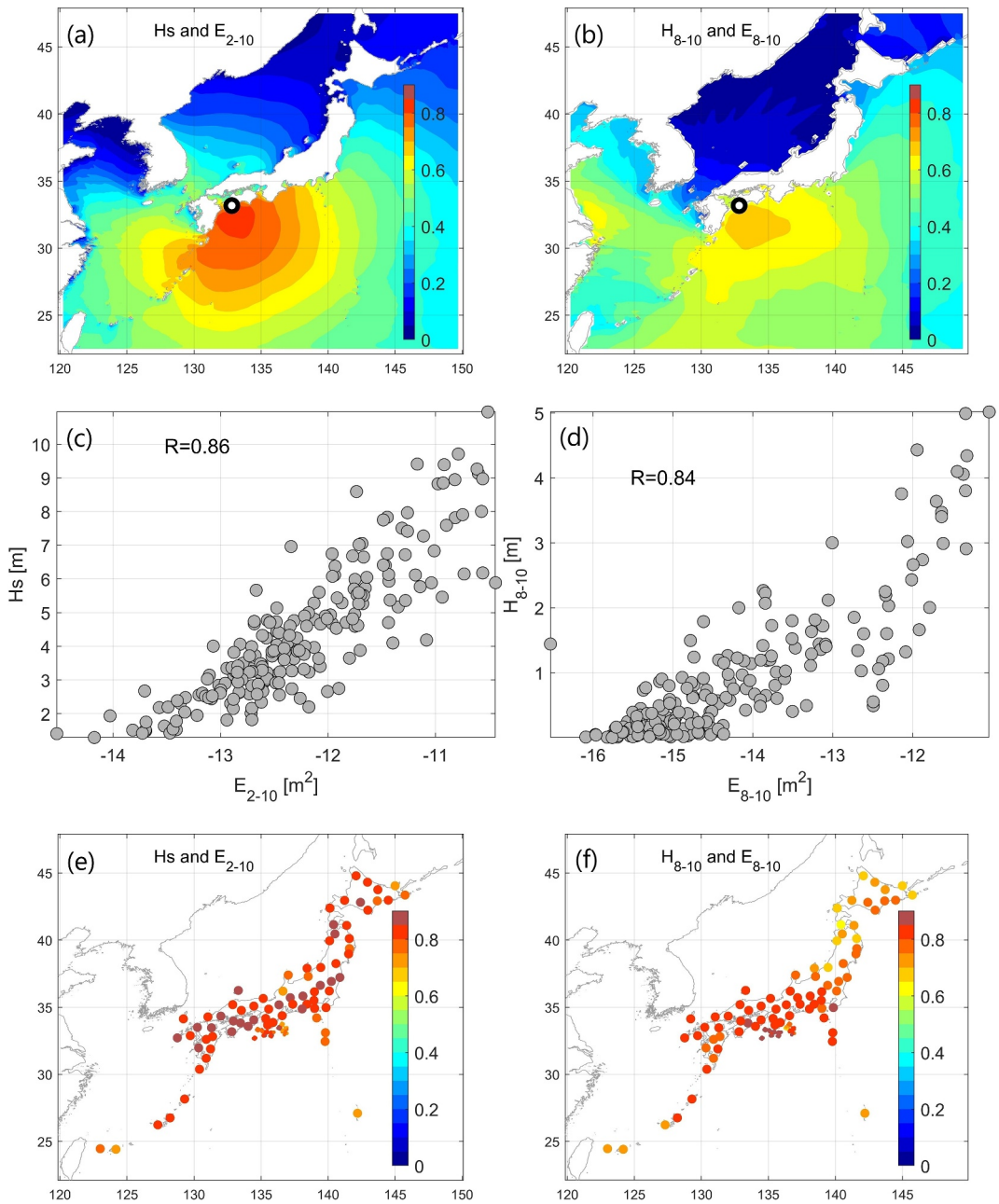

Figure 2. The relationship between microseisms and ocean wave heights. (a) The spatial distribution of the correlation coefficient between hourly E_{2-10} at the TSA location and hourly H_s. (b) Same as (a) but for long-period components (E_{8-10} and H_{8-10}). (c) The relationship between the maximum hourly E_{2-10} at location TSA and the spatially averaged maximum hourly H_s each tropical cyclone events. (d) Same as (c) but for long-period components (E_{8-10} and H_{8-10}). (e) The correlation coefficients between maximum E_{2-10} and the spatially averaged maximum H_s during tropical cyclone events for all seismic stations. (f) Same as (e) but for long-period components (E_{8-10} and H_{8-10}).

3.2. The 20-Year Maximum Events of Microseism Energy

The tropical cyclones that generated the maximum microseisms are identified here. The maximum values that occurred within 10 days were grouped into the same events. Figure 3a shows the maximum microseisms events. In these events, the number of locations with historical maximum microseisms E_{2-10}, was the largest. Location counting was based on F-net locations with a data duration of more than 10 years for a total of 73 locations. The number of locations with the maximum value of the E_{2-10} during 6UTC 11 to 6UTC 21 October 2013 were 31 out

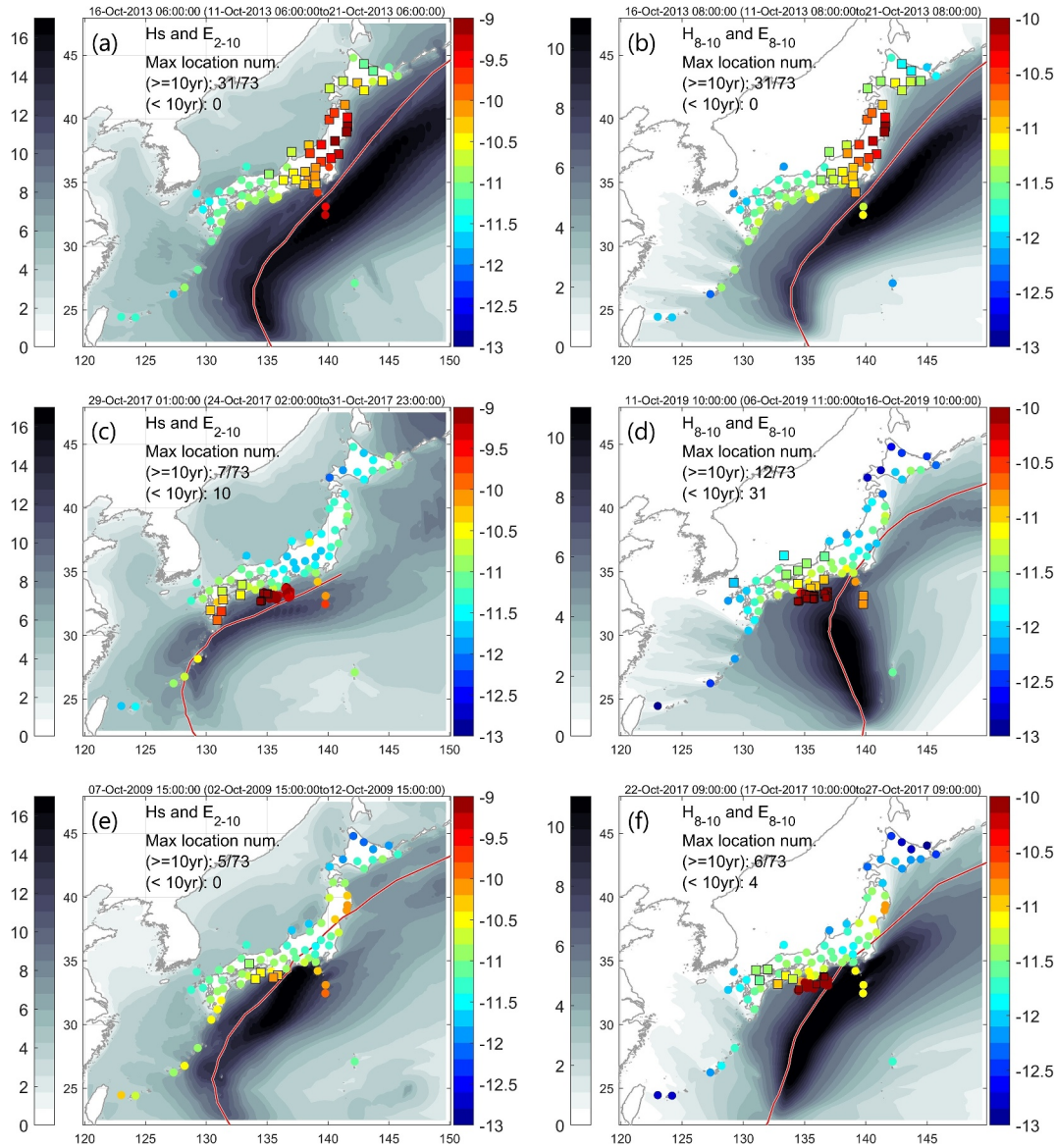

Figure 3. The 20-year maximum events of microseisms. (a, c, e) The three maximum events of E_{2-10}. (b, d, f) The three maximum events of long-period components E_{8-10}. The color scale represents the value of E_{2-10} or E_{8-10} during the events. The seismic stations with the historical maximum value are plotted by black-edged square. The gray color scale represents the maximum H_s or H_{8-10} during the events (unit: m). The events of (a) and (b) are excited by Typhoon Wipha, the event (c) is excited by Saola, (d) is excited by Hagibis, (e) is excited by Melor, and (f) is excited by Lan. The tropical cyclone tracks are plotted by red lines. For the period when ocean-bottom seismic observation (DONET) exists, the data are also plotted in addition to on-land observation (F-net).

of 73 (locations with square markers in Figure 3a). During this period, Typhoon Wipha passed through the domain and recorded a minimum central pressure of 930 hPa. The maximum H_s values during this period are shown in Figure 3a. The wave heights around tropical cyclone track, especially on the right-hand side, were large and reached 18.0 m. For the long-period components, the event in which the number of locations with the maximum E_{8-10} was the largest (Figure 3b), was the same as E_{2-10} (Figure 3a).

The event in which the number of locations was the second- and third-largest differed between E_{2-10} and E_{8-10}. The second- and third-largest event for E_{2-10} was Typhoon Saola in 2017 and Melor in 2009 (Figures 3c and 3e). The numbers of locations with the historical maximum E_{2-10} were seven and five out of 73 during the event. The

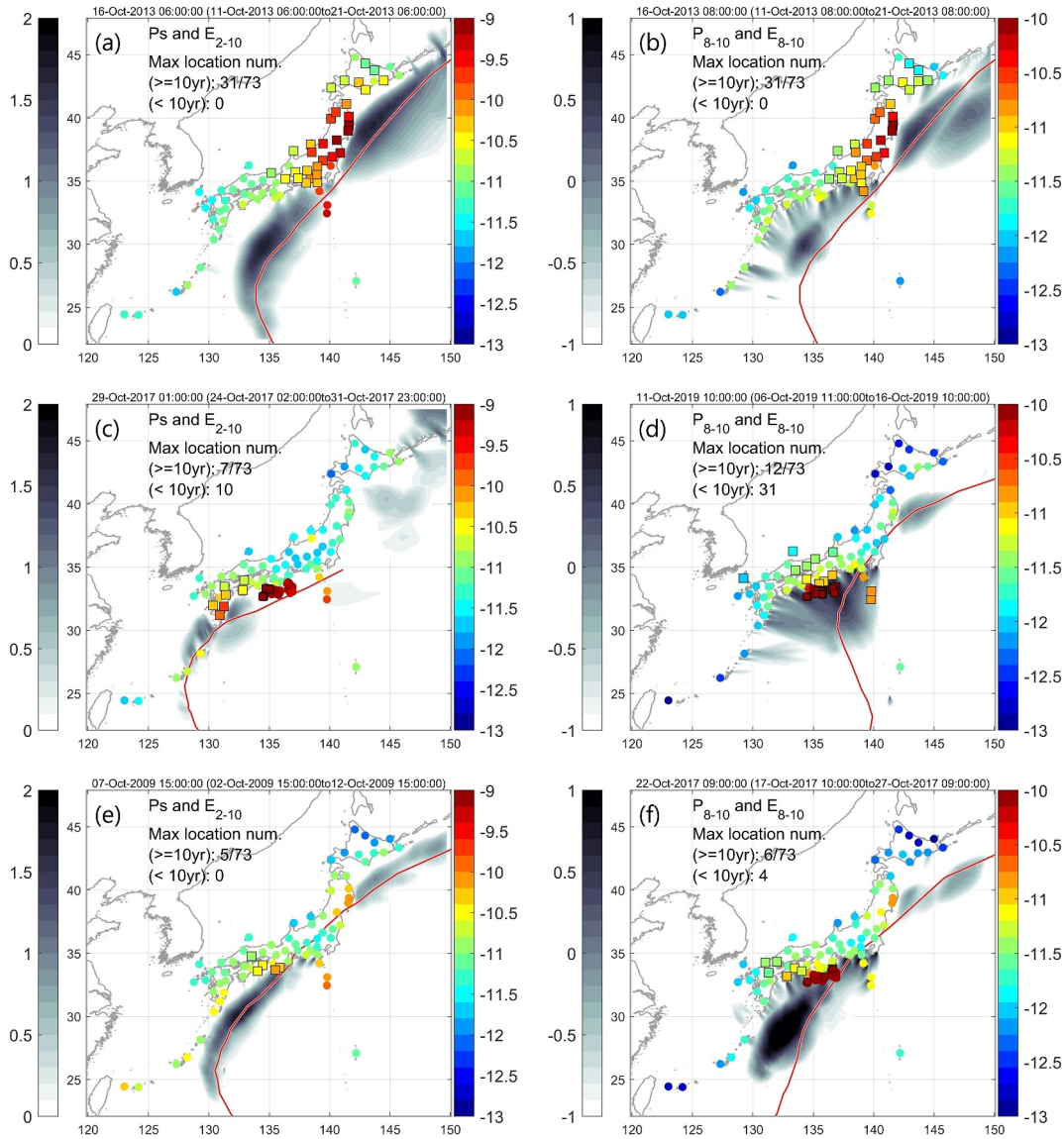

Figure 4. Same as Figure 3 but for wave-induced surface pressures P_s and P_{8-10} not wave heights.

lifetime minimum central pressures of the Saola and Melor were 975 hPa and 910 hPa. Typhoon Saola was not a particularly strong tropical cyclone. As described in the previous section, E_{2-10} is strongly affected by the magnitude of waves closer to a seismic station. Therefore, the reason why the moderate tropical cyclone Saola was identified could be the local large wave occurrence and not the absolute magnitude of the waves generated by the tropical cyclone. Another reason might be that the right combination of wave energy in opposite directions led to large microseisms (Obrebski et al., 2012). However, long-period microseisms can identify the strong tropical cyclones generating ocean waves. Figures 3d and 3f shows the events with the second- and third-largest numbers of locations with a maximum E_{8-10}, which were Typhoons Hagibis in 2019 and Lan in 2017, respectively. The lifetime minimum central pressure of Hagibis and Lan was 915 hPa, indicating that the long-period microseisms were excited by typhoons in the strongest class. The locations with the maximum E_{8-10} were the central (Figure 3d) and western parts (Figure 3f) of Japan for Hagibis and Lan, respectively. The maximum wave heights of H_{8-10} are similar among events Wipha, Hagibis, and Lan, 11.4, 12.1, and 12.9 m, respectively. Typhoon Melor is the fourth event of E_{8-10} which is not shown. Figure 4 shows the same results as Figure 3 but for ocean wave-induced surface pressures P_s and P_{8-10}. The theory (Hasselmann, 1963) says the secondary microseisms are not

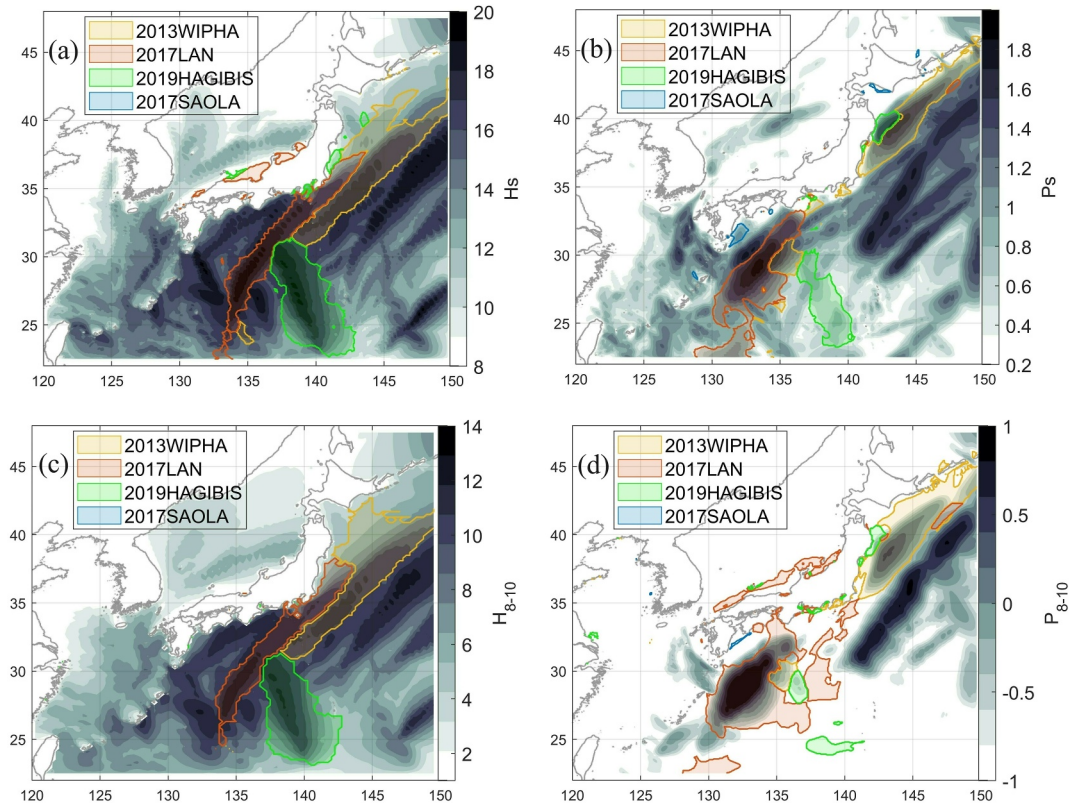

Figure 5. The 20-year maximum values of ocean waves. (a) H_s, (b) P_s, (c) H_{8-10}, and (d) P_{8-10}. The regions where the maximum values are induced by Typhoons Wipha, Lan, Hagibis, and Saola are hatched by each color. The value of P_s and P_{8-10} are shown by $\log_{10}()$.

controlled by magnitude of wave heights itself but for energy in wave components traveling in opposite directions (P_s or P_{t1-t2}). The spatial extents of large P_s or P_{t1-t2} area and large microseisms correspond each other.

3.3. The 20-Year Highest Ocean Wave Events in Ocean Wave Simulations

Section 3.2 shows that maximum secondary microseisms, especially long-period components, are apparently excited by the strongest-class tropical cyclones. From a wave perspective, we derived historical highest-class wave events. Figure 5 shows the spatial distributions of the 20-year maximum waves represented by the wave heights (H_s and H_{8-10}) and wave-induced surface pressures (P_s and P_{8-10}). The three typhoon events derived from the maximum microseisms (E_{8-10}; Figures 3 and 4) were Wipha in 2013, Lan in 2017, and Hagibis in 2019. The regions where the maximum waves occurred during the three events are shown in Figure 5. In addition to the three events, Saola in 2017, which was not a strong tropical cyclone but induced the maximum E_{2-10} as described above, is shown in Figure 5. The historical highest waves and largest wave-induced pressures in the large-scale were generated by three tropical cyclone events, Wipha, Lan, and Hagibis (Figure 5). In particular, the long-period component P_{8-10} (Figure 5d) showed better spatial accordance with the long-period microseisms E_{8-10} (Figures 3b, 3d, and 3f), such as in the eastern, central, and western regions.

The spatial distribution characteristics differed among the three tropical cyclone events. For Wipha and Lan, H_s and H_{8-10} were large (with historical maximum) on the right-hand side of the cyclone tracks and P_s and P_{8-10} were large (with historical maximum) on the left-hand side of the tracks (Figures 3–5). The Hagibis characteristics of P_{8-10} differed from those of Wipha and Lan. The largest location of P_{8-10} was not to the left of the track, but to the northwest of the largest H_{8-10} (Figures 5c and 5d), which was close to the shore and wave propagation direction. This indicates that the largest P_{8-10} was dominated by swell propagation and reflection from the shore rather than by opposing waves under the tropical cyclone.

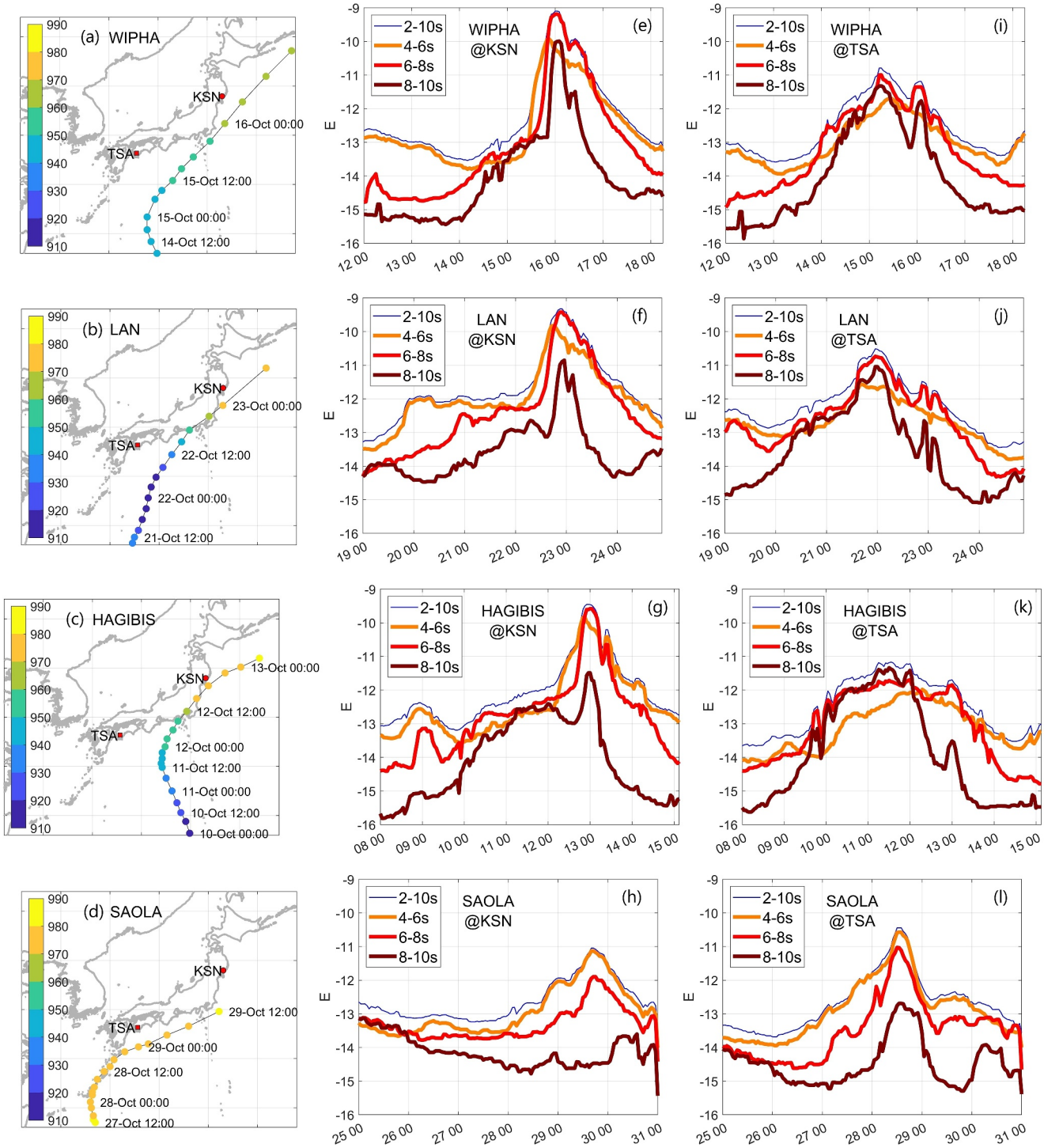

Figure 6. The time series of microseisms (E_{2-10}, E_{4-6}, E_{6-8}, and E_{8-10}) during the historical highest-class tropical cyclone-generated wave events. Top column (a)–(d) shows the tropical cyclone tracks. The color scale indicates the central pressures. Second column (e)–(h) shows the time series at the representative eastern location KSN. Third column (i)–(l) shows the time series at the western location TSA.

The moderate tropical cyclone Saola did not generate the maximum H_s (Figure 5a), but P_s in a limited region (Figure 5b). Furthermore, the footprint of Saola could not be observed in the long-period components (Figures 5c 5d). This is why the maximum E_{2-10} was excited by Saola, whereas E_{8-10} was not. Therefore, the long-period component of microseisms is useful for identifying highest-class wave events.

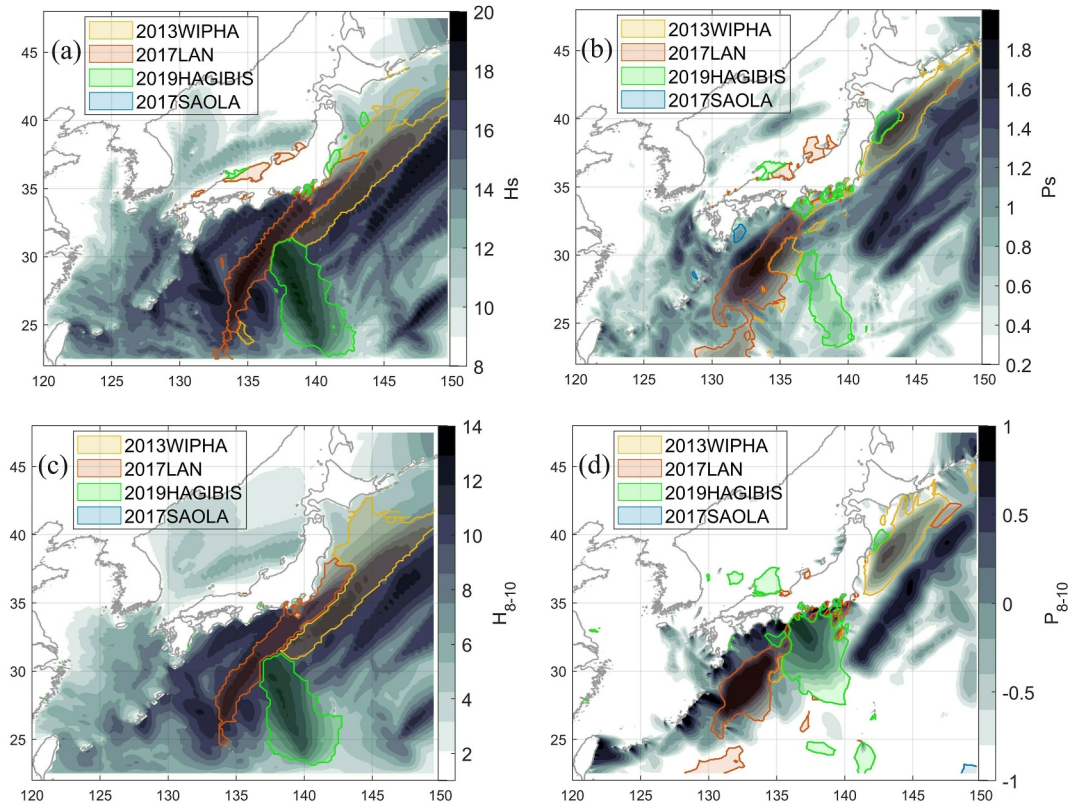

Figure 7. Same as Figure 5 but for the wave simulation without coastal reflection.

3.4. Time Series of Microseisms Depending on Periods

Figure 6 shows the time series of microseism at the two reference locations for each tropical cyclone event: Wipha, Lan, Hagibis, and Saola. Regarding the representative eastern location (KSN), the time series of microseisms showed sharp peaks after the tropical cyclone passed from south to east Japan (Figures 6e–6h). Initially, the short-period components reached their peaks, followed by the long-period components. This indicates wave development physics, which involves a shift from short to long-period wave components during wave development. As tropical cyclones (Figures 6a–6c) make landfall or pass close to Japan, wave development restarts in the eastern ocean of Japan leading to such the sharp peaks.

In contrast, regarding the western location (TSA, Figures 6i–6l), microseisms increased gradually compared with the eastern location (KSN) owing to the gradual development of tropical cyclones and the gradual approach to land in the southern ocean of Japan. In particular, for Hagibis, the long component (E_{8-10}) reached its peak prior to the short component (E_{4-6}). This is because the long components of microseisms during the Hagibis were dominated by swells reflected at the shore, as described above. The sharp peaks observed in the east location (KSN) were also observed in the western location (TSA), excluding the short-period component (E_{4-6}), which dissipated during propagation to the west from the east ocean of Japan.

For Saola in the western location (Figure 6l), the peaks of the shorter period components were superior to those of the other three strong tropical cyclone events. However, the long-period component (E_{8-10}) was much smaller than those of the other three strong tropical cyclone events. This indicates that long-period components can represent the overall intensity of ocean waves generated by tropical cyclones.

4. Discussion

Generally, reflection at the shore is not well considered and is ignored in spectral wave model simulations. This study applied a uniform reflection coefficient (0.1) to all shorelines and wave frequency (Ardhuin &

Roland, 2012). The same wave hindcast was conducted without shoreline reflection. Figure 7 is the same as Figure 5, except for the wave hindcast without reflection. Regarding the wave height, the spatial distributions were the same as those with reflection (Figures 7a and 7c compared with Figures 5a and 5c). Therefore, it is not necessary to consider reflection in the usual wave hindcast that prioritizes the wave height. However, ocean-wave-induced surface pressures are not such situation. For P_s, the value without reflection (Figure 7b) was smaller in areas close to the shoreline, especially on the North Pacific side than that with reflection (Figure 5b). The differences in the long-period component pressure P_{8-10} were clearer than P_s. The Hagibis spatial distributions of P_{8-10} were completely different (Figures 5d and 7d). The regions of historical maximum pressure P_{8-10} disappeared in the simulation without reflection. The previous section showed the importance of swells reflected at the shoreline in the Hagibis event, which was confirmed by comparing simulations with and without reflection. However, the regions of the historical maximum P_{8-10} in Wipha and Lan were not significantly different, with or without reflection. This indicates that opposing swells under tropical cyclones in Wipha and Lan dominated microseism events.

The formulation of air–sea momentum transfer under extreme tropical cyclones has not reached to consensus in meteorological and oceanographic field (Sroka & Emanuel, 2021). The question on whether the drag coefficient of air–sea momentum transfer under tropical cyclone increase, decrease, or constant with wind speed increasing, has not been addressed. The formulation is directly related to ocean wave height development under extreme tropical cyclones (Shimura et al., 2024). Based on the relationship between microseisms and tropical cyclone generated ocean wave heights, we speculate that the microseisms observation can constrain the ocean wave model representation of extreme wave development and then possibly air–sea momentum transfer. Regarding non-linear wave-wave interactions and wave dissipation parameterizations in wave model, Alday and Ardhuin (2023) showed the usefulness of microseism observation.

This study showed the statistical relationship between ocean wave statistics, wave height, wave-induced pressure, and secondary microseisms. Physical explanations of the relationship between wave statistics and local microseism generation require an analysis on local site effects such as ocean surface pressures to ocean bottom pressures conversion depending on wave frequency and water depth, dissipation along microseismic propagation in the crust, which are empirically tuned (Ardhuin et al., 2011). If these effects can be formulated physically rather than empirically, perfect monitoring of tropical cyclone-generated waves from microseisms can be achieved, which is the goal of future studies.

5. Conclusions

This study demonstrated the statistical relationship between tropical cyclone generated ocean wave statistics and secondary microseisms based on 20-year long microseisms by Japanese seismic observation networks and 20-year long high-resolution wave hindcast. Previous studies have focused mainly on source sites of microseisms generated under specific tropical cyclones and not analyzed on the magnitude/intensity of ocean waves under tropical cyclones which is greater interest of disaster mitigation and research on extreme wave physics. Facilitated by using microseism energy within an 8–10 s period compared with 2–10 s, we showed that Typhoon Wipha in 2013, Typhoon Lan in 2017, and Typhoon Hagibis in 2019 were the maximum microseisms energy events in the past 20 years, and were related with the highest ocean waves and largest wave-induced surface pressures simulated by ocean wave model results. Numerical simulations cannot be confirmed by direct wave observations due to lack of observation. However, the high correlation between tropical cyclone-excited microseisms and simulated ocean waves enables us to identify the highest-class ocean wave events based on the observed microseisms. The identification can be useful information for disaster mitigation because the measures need to be established against the highest ocean wave forcing. This study analyzed 20-year microseisms observation. Bromirski (2023) showed that the historical 90-year wave height variability along the California coast based on long-term seismic records in the time without wave records. Similar to the work of Bromirski (2023), the longer records of microseisms have been archived, and the long historical records can help us estimate the highest potential tropical cyclone-generated ocean wave events. For example, Muroto Typhoon in 1934 (Arakawa, 1957) and Typhoon Vera in 1959 (Otao, 1960) caused the worst-class historical coastal disasters in Japan. Although the ocean waves have not been well observed at that time, the microseisms observations existed at some locations, which have a possibility to reveal the extreme wave conditions of such historical worst-class disasters. Furthermore, because microseisms observations contain rich information on the development and propagation of waves depending on wave frequency as shown Section 3.4, we expect that microseisms will help us to monitor the

extreme tropical cyclone waves and understand the physics of extreme waves which are extremely difficult to be observed.

Data Availability Statement

Seismic observation data from F-net (NIED F-net, 2019) and DONET (NIED DONET, 2019) were accessed from the National Research Institute for Earth Science and Disaster Resilience website (https://www.hinet.bosai.go.jp/?lanG=en). Our wave simulation data are available at the ZENODO repository (Shimura, 2024a, 2024b, 2024c, 2024d). The JMA-MSM wind field (JMA, 2024) was accessed from the Research Institute of Sustainable Humanosphere website at Kyoto University (http://database.rish.kyoto-u.ac.jp/arch/jmadata/). The JRA-55 reanalysis (Kobayashi et al., 2015) was accessed from the DIAS (https://search.diasjp.net/en/dataset/JRA55). The WAVEWATCH III spectral wave model (The WAVEWATCH III Development Group, 2019) is available from the GitHub repository (https://github.com/NOAA-EMC/WW3). Tropical cyclone track data (RSMC Tokyo-Typhoon Center, n.d.) are available on the JMA website (https://www.jma.go.jp/jma/jma-eng/jma-center/rsmc-hp-pub-eg/besttrack.html).

Acknowledgments
This study was supported by the JST FOREST Program (JPMJFR205R) and JSPS KAKENHI (23H00196, 23H00191, 24H02225, 23K22873, and 24K00989).

References

Alday, M., Accensi, M., Ardhuin, F., & Dodet, G. (2021). A global wave parameter database for geophysical applications. Part 3: Improved forcing and spectral resolution. *Ocean Modelling*, *166*, 101848. https://doi.org/10.1016/j.ocemod.2021.101848

Alday, M., & Ardhuin, F. (2023). On consistent parameterizations for both dominant wind-waves and spectral tail directionality. *Journal of Geophysical Research: Oceans*, *128*(4), e2022JC019581. https://doi.org/10.1029/2022JC019581

Algué, J. (1900). *Relation entre quelques mouvements microséismiques et l'existence, la position et la distance des cyclones a Manille (Philippines)* (p. 131). [Paris: Gauthier-Villars. 1900].

Arakawa, H. (1957). On typhoon storm tides. *Geofisica pura e applicata*, *38*(1), 231–249. https://doi.org/10.1007/BF01996994

Ardhuin, F., Balanche, A., Stutzmann, E., & Obrebski, M. (2012). From seismic noise to ocean wave parameters: General methods and validation. *Journal of Geophysical Research*, *117*(C5), C05002. https://doi.org/10.1029/2011JC007449

Ardhuin, F., & Herbers, T. H. (2013). Noise generation in the solid Earth, oceans and atmosphere, from nonlinear interacting surface gravity waves in finite depth. *Journal of Fluid Mechanics*, *716*, 316–348. https://doi.org/10.1017/jfm.2012.548

Ardhuin, F., Rogers, E., Babanin, A. V., Filipot, J. F., Magne, R., Roland, A., et al. (2010). Semiempirical dissipation source functions for ocean waves. Part I: Definition, calibration, and validation. *Journal of Physical Oceanography*, *40*(9), 1917–1941. https://doi.org/10.1175/2010JPO4324.1

Ardhuin, F., & Roland, A. (2012). Coastal wave reflection, directional spread, and seismoacoustic noise sources. *Journal of Geophysical Research*, *117*(C11), C00J20. https://doi.org/10.1029/2011JC007832

Ardhuin, F., Stutzmann, E., Schimmel, M., & Mangeney, A. (2011). Ocean wave sources of seismic noise. *Journal of Geophysical Research*, *116*(C9), C09004. https://doi.org/10.1029/2011JC006952

Aster, R. C., Ringler, A. T., Anthony, R. E., & Lee, T. A. (2023). Increasing ocean wave energy observed in Earth's seismic wavefield since the late 20th century. *Nature Communications*, *14*(1), 6984. https://doi.org/10.1038/s41467-023-42673-w

Bromirski, P. D. (2023). Climate-induced decadal ocean wave height variability from microseisms: 1931–2021. *Journal of Geophysical Research: Oceans*, *128*(8), e2023JC019722. https://doi.org/10.1029/2023JC019722

Bromirski, P. D., Duennebier, F. K., & Stephen, R. A. (2005). Mid-ocean microseisms. *Geochemistry, Geophysics, Geosystems*, *6*(4), Q04009. https://doi.org/10.1029/2004GC000768

Emanuel, K. A. (1988). The maximum intensity of hurricanes. *Journal of the Atmospheric Sciences*, *45*(7), 1143–1155. https://doi.org/10.1175/1520-0469(1988)045<1143:TMIOH>2.0.CO;2

Fan, W., McGuire, J. J., de Groot-Hedlin, C. D., Hedlin, M. A., Coats, S., & Fiedler, J. W. (2019). Stormquakes. *Geophysical Research Letters*, *46*(22), 12909–12918. https://doi.org/10.1029/2019GL084217

Gilmore, M. H., & Hubert, W. E. (1948). Microseisms and Pacific typhoons. *Bulletin of the Seismological Society of America*, *38*(3), 195–228. https://doi.org/10.1785/BSSA0380030195

Grevemeyer, I., Herber, R., & Essen, H. H. (2000). Microseismological evidence for a changing wave climate in the northeast Atlantic Ocean. *Nature*, *408*(6810), 349–352. https://doi.org/10.1038/35042558

Gualtieri, L., Camargo, S. J., Pascale, S., Pons, F. M., & Ekström, G. (2018). The persistent signature of tropical cyclones in ambient seismic noise. *Earth and Planetary Science Letters*, *484*, 287–294. https://doi.org/10.1016/j.epsl.2017.12.026

Gualtieri, L., Stutzmann, E., Juretzek, C., Hadziioannou, C., & Ardhuin, F. (2019). Global scale analysis and modelling of primary microseisms. *Geophysical Journal International*, *218*(1), 560–572. https://doi.org/10.1093/gji/ggz161

Hasselmann, K. (1963). A statistical analysis of the generation of microseisms. *Reviews of Geophysics*, *1*(2), 177–210. https://doi.org/10.1029/RG001i002p00177

Hasselmann, K., Barnett, T. P., Bouws, E., Carlson, H., Cartwright, D. E., Enke, K., et al. (1973). Measurements of wind-wave growth and swell decay during the Joint North Sea Wave Project (JONSWAP). *Ergaenzungsheft zur Deutschen Hydrographischen Zeitschrift, Reihe A, Nr. 12*. https://hdl.handle.net/21.11116/0000-0007-DD3C-E

JMA. (2024). Outline of the operational numerical weather prediction at the Japan meteorological agency. Retrieved from https://www.jma.go.jp/jma/jma-eng/jma-center/nwp/outline2024-nwp/index.htm

Kobayashi, S., Ota, Y., Harada, Y., Ebita, A., Moriya, M., Onoda, H., et al. (2015). The JRA-55 reanalysis: General specifications and basic characteristics. *Journal of the Meteorological Society of Japan. Ser. II*, *93*(1), 5–48. https://doi.org/10.2151/jmsj.2015-001

Lin, J., Lin, J., & Xu, M. (2017). Microseisms generated by super typhoon Megi in the western Pacific Ocean. *Journal of Geophysical Research: Oceans*, *122*(12), 9518–9529. https://doi.org/10.1002/2017JC013310

Longuet-Higgins, M. S. (1950). A theory of the origin of microseisms. *Philosophical Transactions of the Royal Society A*, *243*(857), 1–35. https://doi.org/10.1098/rsta.1950.0012

Nakata, N., Gualtieri, L., & Fichtner, A. (Eds.) (2019). Physics of ambient noise generation by ocean waves, *Seismic ambient noise* (pp. 69–108). Cambridge University Press. https://doi.org/10.1017/9781108264808.005

NIED DONET. (2019). National research institute for earth science and disaster resilience [Dataset]. *NIED DONET*. https://doi.org/10.17598/NIED.0008

NIED F-net. (2019). National research institute for earth science and disaster resilience [Dataset]. *NIED F-net*. https://doi.org/10.17598/NIED.0005

Nishida, K., & Takagi, R. (2022). A global centroid single force catalog of P-wave microseisms. *Journal of Geophysical Research: Solid Earth*, *127*(4), e2021JB023484. https://doi.org/10.1029/2021JB023484

Obrebski, M. J., Ardhuin, F., Stutzmann, E., & Schimmel, M. (2012). How moderate sea states can generate loud seismic noise in the deep ocean. *Geophysical Research Letters*, *39*(11), L11601. https://doi.org/10.1029/2012GL051896

Okada, Y., Kasahara, K., Hori, S., Obara, K., Sekiguchi, S., Fujiwara, H., & Yamamoto, A. (2004). Recent progress of seismic observation networks in Japan –Hi-net, F-net, K-NET and KiK-net. *Earth Planets and Space*, *56*(8), xv–xxviii. https://doi.org/10.1186/BF03353076

Otao, H. (1960). A brief outline of the Ise-wan typhoon. *Coastal Engineering Proceedings*, *1*(7), 54. https://doi.org/10.9753/icce.v7.54

Park, S., & Hong, T. K. (2020). Typhoon-induced microseisms around the South China Sea. *Seismological Research Letters*, *91*(6), 3454–3468. https://doi.org/10.1785/0220190310

Poppeliers, C., & Mallinson, D. (2015). High-frequency seismic noise generated from breaking shallow water ocean waves and the link to time-variable sea states. *Geophysical Research Letters*, *42*(20), 8563–8569. https://doi.org/10.1002/2015GL066126

Rappaport, E. N. (2014). Fatalities in the United States from Atlantic tropical cyclones: New data and interpretation. *Bulletin of the American Meteorological Society*, *95*(3), 341–346. https://doi.org/10.1175/BAMS-D-12-00074.1

Retailleau, L., & Gualtieri, L. (2019). Toward high-resolution period-dependent seismic monitoring of tropical cyclones. *Geophysical Research Letters*, *46*(3), 1329–1337. https://doi.org/10.1029/2018GL080785

Retailleau, L., & Gualtieri, L. (2021). Multi-phase seismic source imprint of tropical cyclones. *Nature Communications*, *12*(1), 2064. https://doi.org/10.1038/s41467-021-22231-y

RSMC Tokyo-Typhoon Center. (n.d.). RSMC best track data [Dataset]. *RSMC Tokyo-Typhoon Center*. Retrieved from https://www.jma.go.jp/jma/jma-eng/jma-center/rsmc-hp-pub-eg/besttrack.html

Shimura, T. (2024a). Data for "The 20-year highest tropical cyclone-generated waves associated with the maximum energy of seismic noises" (Subset 1) [Dataset]. *Zenodo*. https://doi.org/10.5281/zenodo.11495405

Shimura, T. (2024b). Data for "The 20-year highest tropical cyclone-generated waves associated with the maximum energy of seismic noises" (Subset 2) [Dataset]. *Zenodo*. https://doi.org/10.5281/zenodo.11495407

Shimura, T. (2024c). Data for "The 20-year highest tropical cyclone-generated waves associated with the maximum energy of seismic noises" (Subset 3) [Dataset]. *Zenodo*. https://doi.org/10.5281/zenodo.11495368

Shimura, T. (2024d). Data for "The 20-year highest tropical cyclone-generated waves associated with the maximum energy of seismic noises" (Subset 4) [Dataset]. *Zenodo*. https://doi.org/10.5281/zenodo.11652369

Shimura, T., & Mori, N. (2019). High-resolution wave climate hindcast around Japan and its spectral representation. *Coastal Engineering*, *151*, 1–9. https://doi.org/10.1016/j.coastaleng.2019.04.013

Shimura, T., Mori, N., & Miyashita, T. (2024). Footprint of the air-sea momentum transfer saturation observed by ocean wave buoy network in extreme tropical cyclones. *Coastal Engineering*, *191*, 104537. https://doi.org/10.1016/j.coastaleng.2024.104537

Sroka, S., & Emanuel, K. (2021). A review of parameterizations for enthalpy and momentum fluxes from sea spray in tropical cyclones. *Journal of Physical Oceanography*, *51*(10), 3053–3069. https://doi.org/10.1175/JPO-D-21-0023.1

Sufri, O., Koper, K. D., Burlacu, R., & de Foy, B. (2014). Microseisms from superstorm sandy. *Earth and Planetary Science Letters*, *402*, 324–336. https://doi.org/10.1016/j.epsl.2013.10.015

Takagi, R., Nishida, K., Maeda, T., & Obara, K. (2018). Ambient seismic noise wavefield in Japan characterized by polarization analysis of Hi-net records. *Geophysical Journal International*, *215*(3), 1682–1699. https://doi.org/10.1093/gji/ggy334

The WAVEWATCH III Development Group. (2019). User manual and system documentation of WAVEWATCH III version 6.07 [Software]. *Tech. Note 333. NOAA/NWS/NCEP/MMAB.465*. https://doi.org/10.2151/jmsj.2015-001

Traer, J., Gerstoft, P., Bromirski, P. D., & Shearer, P. M. (2012). Microseisms and hum from ocean surface gravity waves. *Journal of Geophysical Research*, *117*(B11), B11307. https://doi.org/10.1029/2012JB009550

Zhang, J., Gerstoft, P., & Bromirski, P. D. (2010). Pelagic and coastal sources of P-wave microseisms: Generation under tropical cyclones. *Geophysical Research Letters*, *37*(15), L15301. https://doi.org/10.1029/2010GL044288